ACS Catalysis

Research Article

pubs.acs.org/acscatalysis

Palladium–Tin Alloyed Catalysts for the Ethanol Oxidation Reaction in an Alkaline Medium

Wenxin Du,[†] Kayla E. Mackenzie,[†] Daniel F. Milano,[†] N. Aaron Deskins,[‡] Dong Su,[§] and Xiaowei Teng*[,†]

[†]Department of Chemical Engineering, University of New Hampshire, Durham, New Hampshire 03824, United States

[‡]Department of Chemical Engineering, Worcester Polytechnic Institute, Worcester, Massachusetts 01609, United States

[§]Center for Functional Nanomaterials, Brookhaven National Laboratory, Upton, New York 11973, United States

Supporting Information

ABSTRACT: In this paper, we present a study of a series of carbon-supported Pd–Sn binary alloyed catalysts prepared through a modified Polyol method as anode electrocatalysts for direct ethanol fuel cell reactions in an alkaline medium. Transmission electron microscopy, energy-dispersive X-ray spectroscopy, X-ray diffraction, X-ray photoelectron spectroscopy, and aberration-corrected scanning transmission electron microscopy equipped with electron energy loss spectroscopy were used to characterize the Pd–Sn/C catalysts, where homogeneous Pd–Sn alloys were determined to be present with the surface Sn being partially oxidized. Among various Pd–Sn catalysts, $Pd_{86}Sn_{14}$/C catalysts showed much enhanced current densities in cyclic voltammetric and chronoamperometric measurements, compared to commercial Pd/C (Johnson Matthey). The overall rate law of ethanol oxidation reaction for both $Pd_{86}Sn_{14}$/C and commercial Pd/C were also determined, which clearly showed that $Pd_{86}Sn_{14}$/C was more favorable in high ethanol concentration and/or high pH environment. Density functional theory calculations also confirmed Pd–Sn alloy structures would result in lower reaction energies for the dehydrogenation of ethanol, compared to the pure Pd crystal.

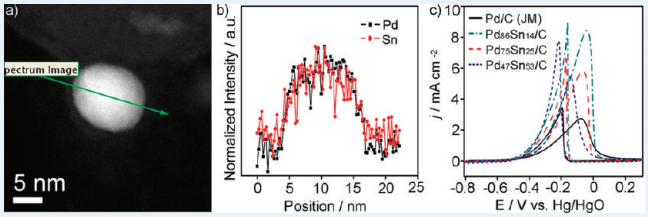

KEYWORDS: *Pd–Sn, ethanol oxidation reaction, alkaline fuel cell, rate law, DFT calculations*

1. INTRODUCTION

Demand for energy, coupled with concerns over environmental pollution and growing fossil fuel costs has created a great need for clean and efficient power sources for the nation. Since a major source of carbon emissions in the United States is the transportation system, a practical path to achieve significant emissions reductions is to find alternative fuels to gasoline, as well as alternative power devices to the internal combustion engine from which thermodynamic efficiency is subject to Carnot cycle limitation (typically <35%).[1] Over the past forty years, a great deal of attention has gone into developing low–temperature fuel cells, devices that can directly electro-oxidize small organic molecules (SOMs) for electricity with a high thermodynamic efficiency (up to 97%), and provide an alternative path to power.[2,3]

Ethanol has many advantages over hydrogen, methanol, and formic acid as a fuel in fuel cells, though the latter three are by far the most studied fuels in fuel cells research. Ethanol has a lower toxicity, and contains a higher energy density. Furthermore, it has a higher boiling point for safer storage in transportation applications. More importantly, ethanol can be produced in large quantities by fermentation of sugar–containing and/or cellulose–containing raw materials, and thus it has been recognized as a substantial energy source in the future of "green" technology.[4−7] At present, direct ethanol fuel cells (DEFCs) are mostly using acidic proton exchange membranes (PEMs), because PEMs have high proton conductivity and mechanical stability and the generated CO_2 can be easily removed.[3,7,8]

However, despite all potential advantages, oxidation of SOMs, including ethanol, in PEM fuel cells generally shows slow kinetics. Several in situ measurements show that during the ethanol oxidation reaction (EOR), various strongly adsorbed intermediates are produced such as acetaldehyde, acetic acid, and carbon monoxide,[9−11] which poison active sites on the surface of catalysts, and reduce the fuel cell efficiency considerably. Thus improving the EOR activity is vital to enhance the DEFC performance. On the other hand, the kinetics of oxidation of SOMs can be dramatically enhanced using alkaline media via so-called alkaline fuel cells (AFCs). In an AFC, the overpotential loss is considerally smaller than that in acidic electrolyte.[12,13] Moreover, the abundance of adsorbed hydroxyl groups (*OH) on the catalyst surface leads to the poisoning effect of carbonyl species being weak compared to that in PEM fuel cells. Recent progress in solid alkaline anion exchange membranes also stimulates a resurgence of interest in AFCs.[14,15]

Received: November 16, 2011
Revised: January 1, 2012
Published: January 10, 2012

As one of the platinum group metals, Pd shows great potential in electrocatalysis as an anode catalyst, not only because of its similar catalytic properties to Pt counterparts but also because of its low material cost compared to Pt. In particular, the abundance of Pd on the Earth's crust is higher than Pt, making it very attractive for long-term industrial applications. Among several pure metals, Pd is the more active catalyst for the EOR in alkaline media than Pt.[16] Alloyed and oxide supported Pd-M (M: Ru, Au, Ni, Ag, Sn, Ir, and Ti) binary electrocatalysts have been widely reported in the literature.[16−27] Substantial efforts have been devoted to the systematic manipulation of the chemical composition and structure of Pd-based catalysts for further improvement of the catalytic performance of the EOR. However, few studies have studied the kinetics study of EOR on Pd-based catalysts in alkaline solutions.

Although Pt−Sn has been considered as one of the best catalysts for the EOR in acidic electrolytes, its Pd-based counterpart (Pd−Sn) has not been well studied for the EOR in alkaline media. Unanswered questions include: what is the optimum Sn content and what is the function of its alloyed (Sn metal) and nonalloyed (SnO_2) phases? The EOR in general has not been well understood, not only in alkaline electrolytes, but also in acidic electrolytes. Results from research groups of Kowal, Adzic, Xin, and Zhou showed that nonalloyed SnO_2 in the vicinity of Pt catalysts could enable oxygen species conveniently to remove the CO-like residues during oxidation of ethanol to free Pt active sites, resulting in a surprising promotion of catalytic activity for ethanol electrooxidation in an acidic elctrolyte.[28−31] On the other hand, Bohm and Aires showed that metallic Sn alloyed with Pt (Pt_3Sn) and Pd will result in better electroactivities for EOR because of both bifunctional effect and electronic modification upon Pt−Sn and Pd−Sn alloy formation in both acidic and alkaline media.[16,30,32] These controversial results, that is, whether alloyed or nonalloyed Pt−Sn and Pd−Sn catalysts have better EOR activities, again underscore the intriguing structure−property relationships at the nanoscale level. The lack of structural and spectroscopic information for Pd−based systems hinders mechanistic interpretation for the EOR. A detailed understanding of the role of alloyed and oxide phases as well as the kinetics and mechanism of ethanol oxidation on Pd−Sn catalysts is crucial to develop a new class of Pd-based catalysts for EOR in alkaline media.

Here, we report the synthesis of various carbon supported Pd−Sn electrocatalysts. Combined techniques verify the homogeneous alloy structure between Pd and Sn. Electrochemical measurements toward EOR further determine the optimum Sn content in Pd−Sn to be 14%. The promotional effect of Sn on the EOR activity is confirmed by kinetics study of the EOR, but also is verified by density functional theory (DFT) calculations.

2. EXPERIMENTAL SECTION

2.1. Synthesis of Pd−Sn/C Catalysts. The carbon supported Pd−Sn electrocatalysts were prepared with a modified sequential Polyol method followed by addition of carbon black (Vulcan XC72R). In a typical synthesis of $Pd_{86}Sn_{14}$ nanocrystals, 33.3 mg of $SnCl_2$ (Alfa Aesar, 99%) was initially dissolved in 12 mL of ethylene glycol (EG, PHARMCO-AAPER, 11 mL) and deionized water solution (1 mL). Then the mixture was heated up to 180 °C to allow reaction for 1 h, resulting in a light yellow tin colloidal solution. In the second step, 26 mg of K_2PdCl_4 (0.08 mmol, Alfa Aesar, 99.99%) was first dissolved in 3 mL of EG solution by bath sonication, and then injected into 8 mL of pre-heated EG (130 °C) in a flask which contained appropriate aliquots of tin (0.02 mmol) colloidal solution. The reaction proceeded for 30 min under argon flow. The as-made $Pd_{86}Sn_{14}$ particles were then mixed with 25 mg of carbon black (Vulcan XC−72) at a stirring rate of 600 revolutions per minute (rpm) for 1 h at room temperature. The resulting carbon-particles slurry was washed with copious ethanol and acetone to remove EG before drying out in a vacuum oven. Finally, the carbon supported $Pd_{86}Sn_{14}$ nanocrystals were treated in a hydrogen/argon flow at 205 °C for 1 h to evaporate any possible ethylene glycol residual, and reduce any possible ionic tin. The $Pd_{47}Sn_{53}$/C and $Pd_{75}Sn_{25}$/C were synthesized in the same way with varied amounts of metal precursors and carbon black. Specifically, 0.06 mmol, 0.075 mmol of K_2PdCl_4, and 0.06 mmol, 0.05 mmol, of tin colloids were added for the synthesis of $Pd_{47}Sn_{53}$/C, and $Pd_{75}Sn_{25}$/C, respectively. All the Pd−Sn/C electrocatalysts were designated as 30 wt % metal loading (Pd and Sn) on carbon support. Pd/C was also made in a similar way and used only as reference in X-ray diffraction (XRD) measurement because of its agglomeration during synthesis.

2.2. Structural Characterizations. The high-angle annular dark-field (HAADF) scanning transmission electron microscopy (STEM) images and electron energy loss spectroscopy (EELS) measurements were collected using an aberration-corrected Hitachi HD 2700C equipped with a modified Gatan Enfina ER spectrometer at the Center for Functional Nanomaterials at Brookhaven National Laboratory.[33] Pd $M_{4,5}$ edge (335 eV) and Sn $M_{4,5}$ edge (485 eV) were utilized in EELS measurements. Regular TEM images were taken using a Zeiss/LEO 922 Omega TEM. XRD patterns were recorded by a Bruker AXS instrument equipped with a GADDS (General Area Detector Diffraction System) detector. A Cu Kα X-ray tube was employed as X-ray source. Chemical compositions of Pd−Sn catalysts were determined by PGT Imix-PC energy dispersive X-ray spectroscopy (EDS) system equipped on a scanning electron microscopy machine (Amray 3300FE). The elemental information was collected from a least five different spots for each sample to ensure adequate accuracy in average. X-ray photoelectron spectroscopy (XPS) was conducted using a Kratos Axis HS XPS system with Mg anode as the X-ray source.

2.3. Electrochemical Measurements. The electrochemical measurements were conducted with a CHI 660 single channel electrochemical workstation (CH Instruments). A three-electrode system which was composed of a glassy carbon rotating disk electrode (RDE) as the working electrode, a platinum wire counter electrode, and an Hg/HgO (1 M KOH) reference electrode was employed for the test. The rotating rate of the working electrode was controlled at 1000 rpm. The supported catalysts were dispersed in deionized water to make a 2 mg mL^{-1} suspension by sonication, and 10 μL catalyst ink (containing 3−5 μg of Pd) was drop-cast on the working electrode. Upon drying, 10 μL of Nafion working solution (0.5%, $V_{0.5\ wt\ \%\ Nafion}/V_{water}$= 0.05 mL:10 mL) was further dropped onto the catalyst layer. The stock Nafion 117 solution (Aldrich) used to prepare Nafion working solution was ~5 wt % in a mixture of lower aliphatic alcohols and water. Commercial Pd/C (20 wt %, 50% water wet, Alfa Aesar), denoted as Pd/C (Johnson Matthey, JM), was used as benchmark to compare the catalytic performance (nominal

dx.doi.org/10.1021/cs2005955 | ACS Catal. 2012, 2, 287−297

mass loading on RDE: 3 μg). The blank cyclic voltammetry (CV) were performed only 1 cycle in Argon-purged 0.5 M KOH (99.99%, Alfa Aesar) electrolyte sweeping from −0.8 to 0.3 V at a scan rate of 50 mV s^{-1}. The electrochemically active surface areas (ECSA) were evaluated from integration of the charges during PdO reduction in the cathode scan, assuming a value of 405 $\mu C/cm^2$ for the reduction of PdO monolayer. CV and chronoamperometry measurements (CA) are generally conducted in 0.5 M ethanol/0.5 M KOH electrolyte at room temperature. Other electrolyte concentrations were also used for Pd/C and $Pd_{86}Sn_{14}/C$ to analyze kinetic parameters. Stabilized CV curves were recorded after 10 cycles sweeping between −0.8 V~0.3 V at scan rate of 50 mV s^{-1}. The quasi-steady state polarization curves recorded at a sweep rate of 1 mV s^{-1} by using the Linear Sweep Voltammetry (LSV) technique in different ethanol/KOH solutions were used to derive the Tafel plots (see main-text for details). The electrolyte was deaerated by bubbling argon for 30 min prior to the measurements.

2.4. DFT Calculations. All DFT calculations were performed with a dual basis set, using the Gaussian and plane waves (GPW) method.,[34] as implemented in the CP2K code,[35] Quickstep module. In the GPW method Gaussian functions are used to represent the electronic wave functions, while plane wave functions are used to represent the electron density. We used double-ζ basis sets for the metals (Pd and Sn), and triple-ζ basis sets for C, H, and O. Core electrons were treated by Goedecker−Tetter−Hutter-type pseudopotentials.[36,37] We used the PBE exchange correlation functional for all calculations.[38] All calculations were spin polarized, and the Γ point was used to sample reciprocal space.

We modeled one of the initial steps of ethanol oxidation, or removal of the first H atom from ethanol. The Pd (111) surface was modeled by a cluster (see Figure 13), which had some Pd atoms selectively replaced by Sn. We previously used this method successfully, and agreement between the cluster and slab approach was shown in our previous work.[39]

We used experimental lattice parameters to determine the cluster bond distances, and only the central atoms of the top layer of the cluster were allowed to relax. In total the cluster had 37 atoms in the top layer and 27 atoms in the bottom layer. Adsorption energies were calculated with the following equation:

$$E_{ads} = E_{surf+adsorbate} - E_{baresurf} - E_{adsorbate\text{-}in\text{-}gas.}$$

Reaction energies for H removal were found by this equation:

$$E_{rxn} = E_{surf+ethanol\text{-}fragment} + E_{surf+H} - E_{baresurf} - E_{surf+ethanol}$$

3. RESULTS AND DISCUSSION

3.1. Crystal Structure of Pd−Sn/C. Figure 1 shows typical TEM images of the Pd−Sn/catalysts. All the Pd−Sn particles were distributed in a relatively broad range on the carbon support. Partially agglomerated particles can be readily seen where the Sn amount is relatively low (Figure 1b, 1c). For comparison, typical TEM images of homemade Pd/C and Pd/C (JM) were also shown in Supporting Information, Figure S1. The chemical compositions of the Pd−Sn/C catalysts were determined by EDS as shown in Figure 1d. To further explore the elemental distributions within the carbon supported

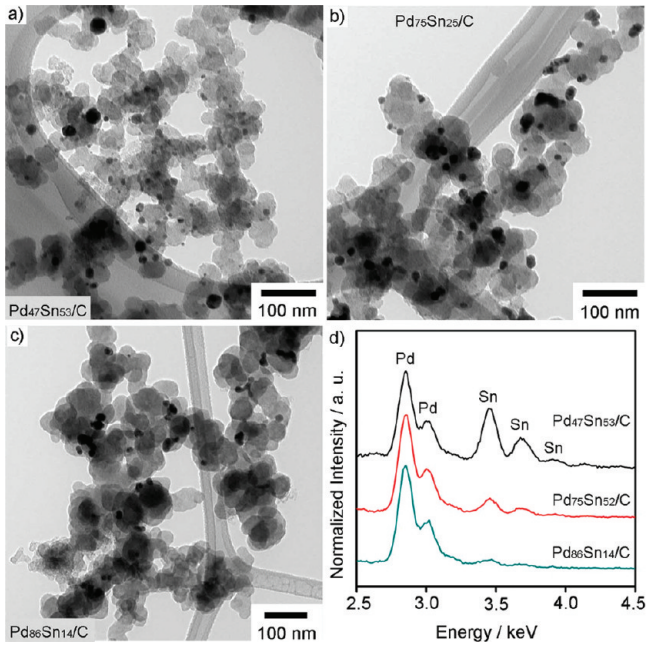

Figure 1. TEM images of (a) $Pd_{47}Sn_{53}/C$, (b) $Pd_{75}Sn_{25}/C$, (c) $Pd_{86}Sn_{14}/C$ electro-catalysts, and (d) their EDS spectra.

nanoparticles, STEM-EELS measurements were performed on several $Pd_{86}Sn_{14}$ particles and the results are quite similar as shown in Figure 2 and Supporting Information, Figure S2. Figure 2 shows the HAADF image of a typical $Pd_{86}Sn_{14}$ particle with the EELS line scans across the particle obtained using aberration-corrected STEM. The normalized intensity profiles of Pd and Sn from two directions marked by green arrows appear typical volcano shapes. Moreover, the concurrently overlapped Pd and Sn intensity profiles strongly indicate that Pd and Sn were evenly distributed throughout the particle, with a homogeneous alloyed nanostructure.

X-ray diffraction (XRD) patterns of $Pd_{47}Sn_{53}/C$, $Pd_{75}Sn_{25}/C$, $Pd_{86}Sn_{14}/C$, and our own synthesized Pd/C are shown in Figure 3. In general, $Pd_{75}Sn_{25}/C$, $Pd_{86}Sn_{14}/C$, and Pd/C showed a typical fcc structure with distinct diffraction peaks attributed to (111), (200), and (220) planes. For example, diffraction peaks of $Pd_{86}Sn_{14}/C$ catalysts appear ~0.2 2θ degrees lower than those of Pd/C (Figure 3b). The $Pd_{75}Sn_{25}/C$ showed dramatic diffraction peak shifting, that is, ~0.3 degree lower than that of Pd/C in (111) peak. This peak shifting can be attributed to the alloy formation between Pd and Sn, as similar expansion of the lattice structure was also reported previously in Pd−Sn, Pt−Sn, and Ir−Sn systems .[11,30,39,40] No Sn or SnO_2 patterns were observed in the $Pd_{86}Sn_{14}/C$ and $Pd_{75}Sn_{25}/C$ catalysts. It is important to point out that the $Pd_{47}Sn_{53}/C$ catalyst showed a distinct orthorhombic pattern. The diffraction peaks at 2θ angles of 38.3, 40.0, 42.5, 46.5, 58.2, 64.1, and 67.3 degrees can be assigned to the Paolovite Pd_2Sn alloy (JCPDS 00-026-1297). The peaks at around 34.5 and 51.1 degrees may be attributed to (101) and (211) planes of SnO_2.

Note that agglomerations of individual nanoparticles would greatly impair the reliability of the particle size distribution solely based on TEM images. Therefore, Scherrer's equation was used to calculate the average size of the Pd−Sn catalysts from (2 2 0) diffraction peaks:

dx.doi.org/10.1021/cs2005955 | ACS Catal. 2012, 2, 287−297

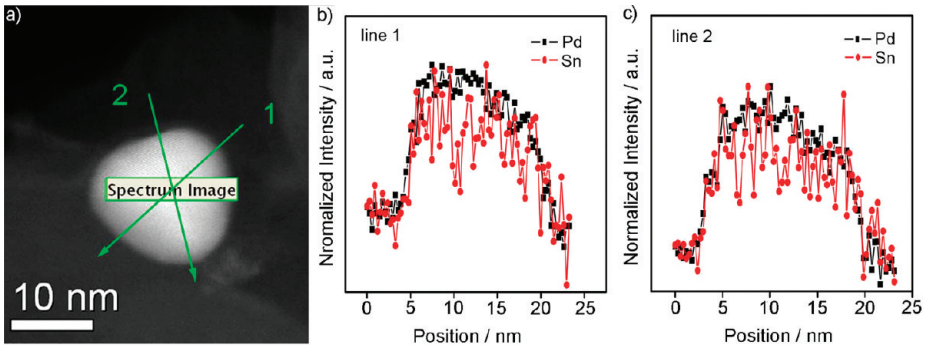

Figure 2. (a) HAADF image of carbon supported individual $Pd_{86}Sn_{14}$ nanoparticle and (b, c) EELS line scans along two different directions of $Pd_{86}Sn_{14}$ particle.

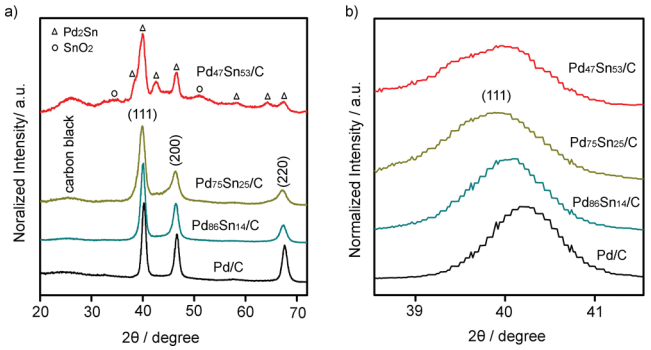

Figure 3. (a) XRD patterns of $Pd_{47}Sn_{53}/C$, $Pd_{75}Sn_{25}/C$, and $Pd_{86}Sn_{14}/C$ along with homemade Pd/C and (b) enlarged pattern around Pd (111) peak.

$$d = \frac{0.9\lambda}{\beta \cos \theta}$$

where λ is the wavelength of X-ray (1.54056 Å), β is the full width at half-maximum (fwhm) of the diffraction peaks in radians, and θ is the Bragg angle at peak position. The (220) diffraction peaks were used to calculate Pd−Sn and Pd crystallite sizes (Table 1). We note that the sizes of catalysts calculated by XRD are considerably smaller than what we expected from TEM images in Figure 1. Since Scherrer's equation is used to estimate the size of single crystal particles, the discrepancy between XRD and TEM results indicate that the large catalyst observed in TEM are the agglomeration of single crystal particles.

The XPS data in Figure 4 further shows that the binding energy of Sn $3d_{5/2}$ and $3d_{3/2}$ for all of the Pd−Sn catalysts are higher than those of metallic Sn (485.0 and 493.4 eV, respectively), indicating the presence of ionic Sn (SnO or SnO_2) on the surface of Pd−Sn catalysts. The Sn on the surface

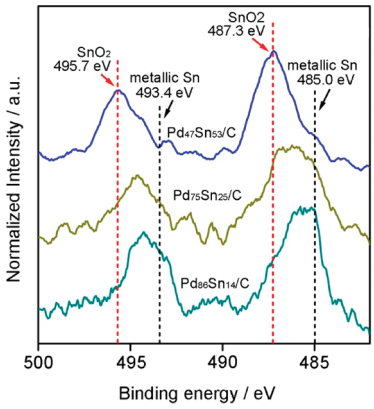

Figure 4. XPS of Sn 3d spectra of $Pd_{47}Sn_{53}/C$, $Pd_{75}Sn_{25}/C$, and $Pd_{86}Sn_{14}/C$. The Sn $3d_{5/2}$ and $3d_{3/2}$ binding energies for both standard Sn and SnO_2 from the database are given by dashed lines.

of $Pd_{86}Sn_{14}/C$ appears to be the least oxidized as the binding energy of Sn $3d_{5/2}$ (~485.6 eV, see Table 1) is closer to that of metallic Sn; on the other hand, Sn on the surface of $Pd_{47}Sn_{53}/C$ was completely oxidized into SnO_2 as the binding energies matches those of the SnO_2 standard perfectly. Combined with STEM-EELS, XRD, and XPS data, we conclude that Pd−Sn/C catalysts are homogeneous alloys with Pd and Sn uniformly distributed throughout an individual catalyst, while the Sn atoms on the surface with the surface Sn are partially oxidized into SnO_2. Note that a similar alloy/metal oxide core-shell configuration has also been identified in Ir−Sn nanocatalysts we reported previously.[39]

3.2. CV and CA Measurement. The cyclic voltammetry (CV) of Pd−Sn/C and commercial Pd/C (JM) catalysts was first investigated in the 0.5 M KOH aqueous solution as shown in Figure 5. All the Pd−Sn/C catalysts appear to have similar columbic features compared to the Pd/C, such as formation

Table 1. Results Obtained for Ethanol Electro-Oxidation on Different Pd−Sn Catalysts

				CV			CA	
catalysts	XRD size (nm)	binding energy of Sn $3d_{5/2}$ (eV)[a]	ECSA (cm^2)	E_p (V vs Hg/HgO)	j_p (mA cm^{-2})	j at −0.1 V (mA cm^{-2})[b]	j at −0.1 V at 2 h (μA cm^{-2})[c]	Tafel slope (mV dec^{-1})
Pd/C (JM)	4.1		2.01	−0.08	2.7	2.6	50.1	187
$Pd_{86}Sn_{14}/C$	6.4	485.6	0.62	−0.04	8.4	6.8	68.7	162
$Pd_{75}Sn_{25}/C$	4.8	486.2	0.66	−0.07	5.8	5.3	50.0	142
$Pd_{47}Sn_{53}/C$	7.2	487.3	0.22	−0.14	5.5	2.8	15.5	139

[a] $3d_{5/2}$ of Sn metal is 485.0 eV, $3d_{5/2}$ of SnO_2 is 487.3 eV. [b] Current density at −0.1 V in CV measurements. [c] Current density after 2 h reaction in CA measurements.

dx.doi.org/10.1021/cs2005955 | ACS Catal. 2012, 2, 287−297

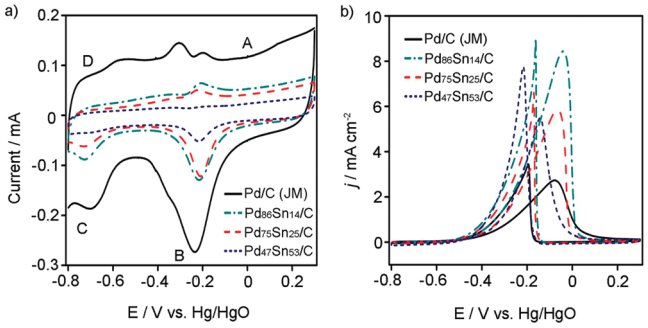

Figure 5. Cyclic voltammetric measurements obtained for $Pd_{47}Sn_{53}$/C, $Pd_{75}Sn_{25}$/C, $Pd_{86}Sn_{14}$/C and Pd/C (JM) in (a) 0.5 M KOH solution and (b) 0.5 M KOH + 0.5 M ethanol solution.

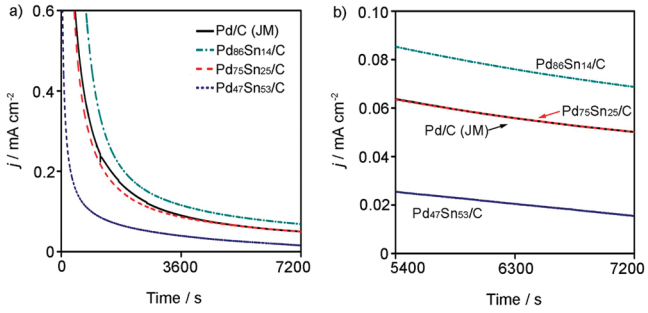

Figure 6. Chronoamperometric measurements (CA) of $Pd_{47}Sn_{53}$/C, $Pd_{75}Sn_{25}$/C, $Pd_{86}Sn_{14}$/C, and Pd/C (JM) in 0.5 M KOH + 0.5 M ethanol solution for 2 h.

(Region A) and reduction (Region B) of Pd oxide, and absorption (Region C) and desorption (Region D) of hydrogen. In the anodic scans, all Pd–Sn/C catalysts show positive shifting of peak potentials compared to Pd/C (JM), while in the cathodic scans, all Pd–Sn/C catalysts also show more positive shifting of the cathodic peak potentials. The distinct anodic (oxidation) and cathodic (reduction) behaviors on Pd–Sn/C and Pd/C (JM) catalysts indicate that the electronic structure on the surface of Pd–Sn has changed after alloying with Sn. In the Pd–Sn homogeneous alloys, electron back-donation from Sn sites to Pd sites could be attributed to electronic modification of Pd structure. The electrochemical active surface area (ECSA) of the all the catalysts was evaluated by the coulometric charge associated with the reduction of Pd oxide as summarized in Table 1.

The electrocatalytic activities of commercial Pd/C (JM), and $Pd_{47}Sn_{53}$/C, $Pd_{75}Sn_{25}$/C, $Pd_{86}Sn_{14}$/C for the EOR were characterized by the CV technique in the mixture of 0.5 M KOH and 0.5 M ethanol aqueous solution. The results normalized by electrochemical active surface area (ECSA) are summarized in Figure 5b and Table 1. We conclude that the order of peak current density for the EOR is $Pd_{86}Sn_{14}$ > $Pd_{75}Sn_{25}$ > $Pd_{47}Sn_{53}$ > Pd (JM). Although $Pd_{47}Sn_{53}$/C shows the lowest current density among all Pd–Sn/C catalysts, it shows the least peak potential, approximately 60 mV more negative than that of Pd/C (JM), which can be attributed to the high degree of Pd–Sn alloying, which changes the electronic structure of Pd dramatically. Such electronic modification may decrease the activation barrier of the EOR, and result in the lower peak potential.[41]

Chronoamperometry (CA) was employed in a solution of 0.5 M KOH and 0.5 M ethanol with a constant applied potential of −0.1 V to evaluate the stability of the Pd–Sn/C catalysts. As displayed in Figure 6, initial rapid decreases in current density were observed for all of the catalysts, which could be ascribed to the accumulation of strongly adsorbed reaction intermediates on the surface active sites. Subsequently, the current decreased slowly and reached a pseudosteady state. From Figure 6 we conclude that the activity order of EOR in term of the current density is $Pd_{86}Sn_{14}$ > $Pd_{75}Sn_{25}$ ≈ Pd > $Pd_{47}Sn_{53}$. In particular, $Pd_{86}Sn_{14}$/C catalyst shows 1.4 times higher current density than Pd/C (JM) after 2 h reaction. Both CV and chronoamperometric measurements conclude that $Pd_{86}Sn_{14}$/C has optimal EOR activity among Pd/C (JM) and other Pd–Sn alloys.

To estimate the alloying effect of Pd–Sn in EOR, the electroactivities of as-made $Pd_{86}Sn_{14}$/C alloyed catalyst, and $Pd_{86}Sn_{14}$/C oxidized at 250 °C (in the air for 1 h) were compared (Supporting Information, Figure S3). The current density of oxidized $Pd_{86}Sn_{14}$/C only showed 10% of the value displayed by $Pd_{86}Sn_{14}$/C alloyed catalyst in CV measurements, and it eventually dropped to zero after 1.5 h in CA measurement.

The promotional effect of Sn in Pd–Sn catalysts in the EOR can be explained by the bifunctional effect, in which Sn and/or SnO_x have stronger interactions with hydroxyl group (OH_{ads}) while Pd has excellent properties in the adsorption and dissociation of ethanol. Such a synergetic effect yields a more active binary catalyst than their monometallic counterparts. However, higher Sn content will also decrease the occupancy of active Pd atoms on the surface, and consequently impair the overall performance of dissociation of adsorbed ethanol. Therefore, an optimal Sn content will be observed as a result of such rival effects of Sn when alloying with Pd. On the other hand, the electronic effect due to the Pd–Sn alloy formation seems to be less important in the overall catalytic performance because $Pd_{86}Sn_{14}$/C showed the least degree of alloy formation compared with the rest of two Pd–Sn catalysts. Although optimal Sn content in Pt–Sn in acid medium has been studied, composition effect in Pd–Sn has not been well studied in alkaline media. For example, Antolini recently predicted the theoretically optimized Sn content for the EOR in partially alloyed Pt_x-Sn/C catalysts for the x in the range from 1.66 to 3, representing 25–38% Sn.[42] Our recent results showed that Sn contents of ∼36% (in the ternary PtRhSn alloys) and ∼20% (in Ir–Sn binary alloys) might be the optimal ratio for the EOR in an acid medium.[39,43] In the current study, an optimal Sn ratio of 14% in Pd–Sn catalysts in an alkaline medium is considerably lower than that of PtSn and Ir–Sn system in an acid medium. This can be explained by the fact that in an alkaline medium Pd can interact with OH_{ads} easier than Ir or Pt in an acid medium. The intermediates of the EOR on the Pd sites will be easier oxidized by adjacent adsorbed OH's which are abundant in an alkaline medium, without the necessity of a relatively high Sn content in acid medium, where OH comes from the strong interaction between Sn and water.

3.3. Tafel Measurement and Final Product Analysis.

Figure 7 shows a linear region of the Tafel plots (kinetics current density as a function of potential) measured in the solution of 0.5 M KOH and 0.5 M ethanol with a scan rate of 1 mV s^{-1} of Pd/C (JM) and the Pd–Sn/C catalysts. The linear region of the Tafel plots stretches from −0.5 to −0.2 V. As the potential is further increased above −0.2 V, the Tafel plot becomes curved, indicating the EORs are no longer charge-transfer controlled reactions. Tafel slopes derived from the linear region are summarized in Table 1, from which three Pd–

dx.doi.org/10.1021/cs2005955 | ACS Catal. 2012, 2, 287–297

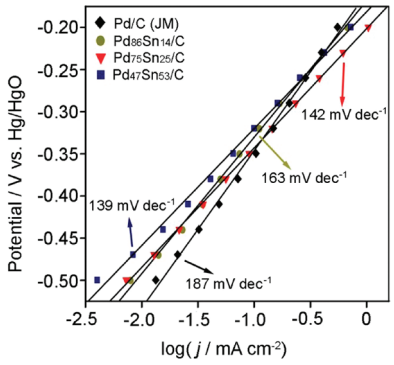

Figure 7. Tafel plot of $Pd_{47}Sn_{53}/C$, $Pd_{75}Sn_{25}/C$, $Pd_{86}Sn_{14}/C$, and Pd/C (JM) in 0.5 M KOH + 0.5 M ethanol solution.

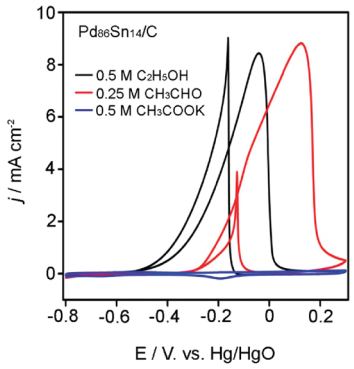

Figure 8. Comparisons of cyclic voltammograms of $Pd_{86}Sn_{14}/C$ for the oxidation of acetaldehyde (CH_3CHO, 0.25 M), acetic acid (CH_3COOH, 0.5 M), and ethanol (CH_3CH_2OH, 0.5 M) in 0.5 M KOH solution.

Sn catalysts showed the slopes ranging from 139 to 162 mV dec^{-1}, appreciably lower than that of Pd/C (JM) (187 mV dec^{-1}). Lower Tafel slopes indicate that the charge-transfer kinetics of the EOR on the Pd−Sn/C catalysts were faster than that on Pd/C (JM) in the alkaline medium. Moreover, Tafel slopes decreased appreciably with the presence of Sn in the catalysts. The lowest Tafel slope was found in $Pd_{47}Sn_{53}/C$ (139 mV dec^{-1}) that contained the highest Sn ratio. Since Sn has a strong interaction with electrolyte to form oxygenated species (e.g., OH_{ads}), it will help the oxidation of the reaction intermediates that adsorbed on the Pd sites and result in faster charge-transfer kinetics.

Previous studies showed controversial results of Tafel slope values on different types of Pd electrodes. Shen et al. reported the Tafel slope of EOR for carbon supported Pd catalyst was 188 mV dec^{-1} and argued that the interference of mass transport in the charge transfer region should be taken into account, while Liang et al. demonstrated that a polycrystalline Pd electrode only had a Tafel slope of 130 mV dec^{-1} during the EOR at low potential range, which is close to the theoretical value (120 mV dec^{-1}).[32,44,45] The Tafel slope of Pd/C (JM) we report here is in good agreement with Shen's report,[44] suggesting a similar mechanism may govern the charge transfer kinetics, though more delicate derivations might be needed to fully interpret the discrepancy in charge transfer kinetics at different Pd electrodes. Liang et al. also found out at low potentials both OH_{ad} (*OH) and ethoxy ($*CH_3CO$) followed the Temkin-type adsorption, indicating that reaction (CH_3CO + OH→ CH_3COOH) is the rate-determining-step for the EOR.[45]

To further analyze the final product of the EOR on Pd−Sn/C, cyclic voltammograms in 0.5 M KOH solutions containing ethanol, acetaldehyde, and potassium acetate are compared. Figure 8 shows that the electro-oxidation of acetaldehyde has similar features compared to that of ethanol, but a slightly higher current density and significant positively shifted peak potential. On the other hand, no distinct oxidation current is observed in the potassium acetate solution. Similar results have been obtained using the Pd disk electrode.[45]

Complete oxidation of ethanol is a complex 12-electron transfer reaction. In situ FTIR results from Bianchini and Zhou indicated the ability of Pd for breaking the C−C bond of ethanol was slightly better than that of Pt under the same conditions,[46,47] showing that the overall selectivity for ethanol oxidation to CO_2 (as CO_3^{2-} in alkaline media) was still low (around 2.5%). According to the in situ FTIR study of the ethanol oxidation in alkaline media, the mechanism of the EOR on the surface of polycrystalline Pd electrode can be expressed as

$$CH_3CH_2OH + 4OH^- \rightarrow CH_3COOH + 4H_2O + 4e^- \quad (1)$$

Our data suggest that acetate salt might be the final product and acetaldehyde is an active intermediate for the EOR on the both Pd/C and Pd−Sn/C catalysts.

3.4. Effects of the Concentrations of Ethanol and KOH on the EOR: the Rate Law. From eq 1, one can conclude that concentrations of both ethanol and KOH will have a dramatic effect on the overall reaction rate of the EOR. Figure 9 shows the CVs of the Pd/C (JM) and $Pd_{86}Sn_{14}/C$ with a constant KOH concentration of 0.5 M and varied ethanol concentrations ranging from 0.05 to 2.0 mol L^{-1}. The oxidation currents obtained from both CV and chronoamperometric (CA) measurements monotonically increase as the ethanol concentration increases. The Tafel plots of $Pd_{86}Sn_{14}/C$ obtained from 0.5 M KOH solution with different ethanol concentrations ranging from 0.05 to 2 M were shown in Figure 10. All curves in this figure are composed of straight lines with two different ranges of slopes. When ethanol concentrations are higher than 0.5 M, the Tafel slopes are around 130 mV dec^{-1}; when ethanol concentrations are lower than 0.5 M, the Tafel slopes are around 160 mV dec^{-1}. These data strongly indicate that there are two mechanisms of EOR which strongly depend on the concentration of ethanol. The slopes of the Tafel plots at high ethanol concentrations are lower (~ 130 mV dec^{-1}), which is in agreement with experimental results using a Pd disk electrode for the EOR in alkaline media.[45]

The effect of ethanol concentration on the EOR can be explained by the competition between the coverage of ethoxy ($*CH_3CO$), resulting from the dehydrogenations of adsorbed ethanol on the surface of the catalysts, and hydroxyl groups (*OH), since the rate-determining step of the EOR is the oxidation of ethoxy ($*CH_3CO$) by the adsorbed hydroxyl (*OH) (eq 4). Because of its strong interaction with hydroxyl groups (OH_{ads}), Sn leads to higher hydroxyl coverage on the surface of Pd−Sn catalysts and lower surface concentration of ethanol than Pd. As ethanol concentration is increased, the intermediate CH_3CO_{ads} (ethoxy) coverage will increase, resulting in the increase of current density and faster charge transfer rate (lower Tafel slopes).

dx.doi.org/10.1021/cs2005955 | ACS Catal. 2012, 2, 287−297

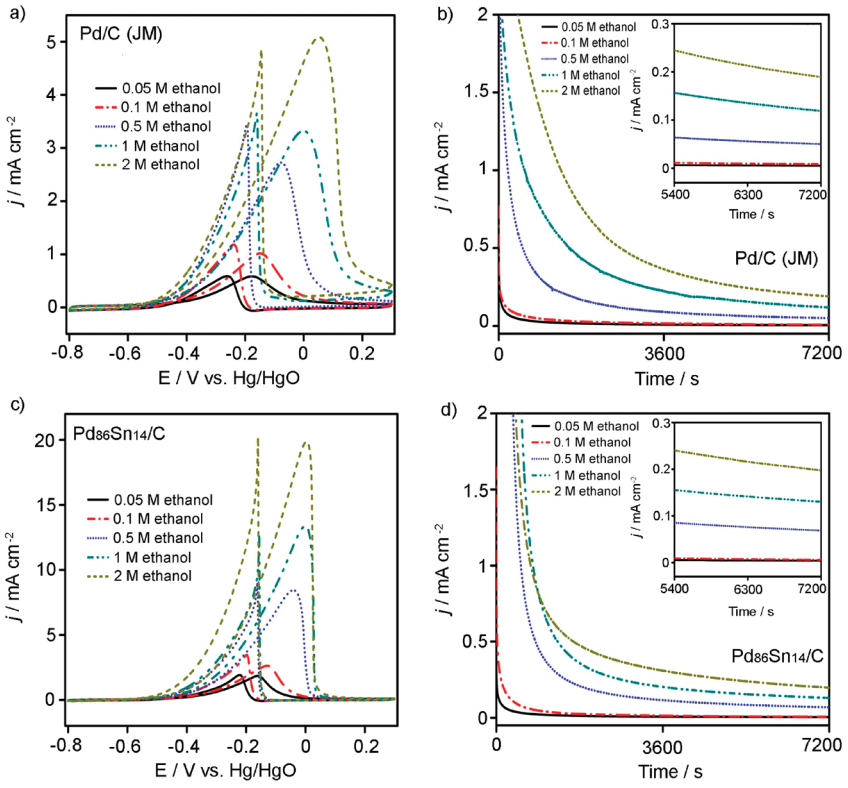

Figure 9. Cyclic voltammetric and chronoamperometric measurements of (a, b) Pd/C (JM) and (c, d) $Pd_{86}Sn_{14}$/C in 0.5 M KOH electrolyte with varied ethanol concentrations.

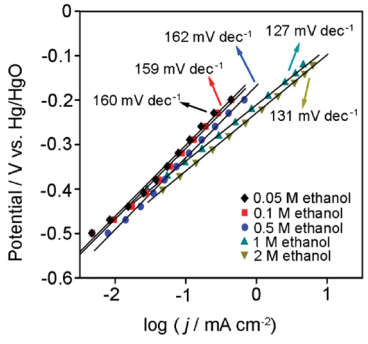

Figure 10. Tafel plot of $Pd_{86}Sn_{14}$/C for ethanol oxidation in 0.5 M KOH with varied ethanol concentrations.

Figure 11 shows the CVs of the Pd/C (JM) and $Pd_{86}Sn_{14}$/C with a constant ethanol concentration of 0.5 M and varied KOH concentration ranging from 0.1 to 2.0 mol L^{-1}. The data show that the peak potentials continuously shift negatively with the increase of KOH concentration. In addition, the peak current density shows a "volcano" shape change with the increase of KOH concentration, that is, it increases as KOH concentration changes from 0.1 to 0.25 M, and gradually drops monotonically once KOH concentration goes higher than 0.25 M. The negative-shift of peak potential as well as the higher current density in higher KOH concentrations at potentials lower than peak potential indicate the oxidation of ethoxy ($*CH_3CO$) in the rate-determining step can be accelerated by increasing the bulk OH^- concentration, which thus favors EOR. However, the decrease of peak current density at higher OH^- concentrations also suggests the ethanol adsorption might be

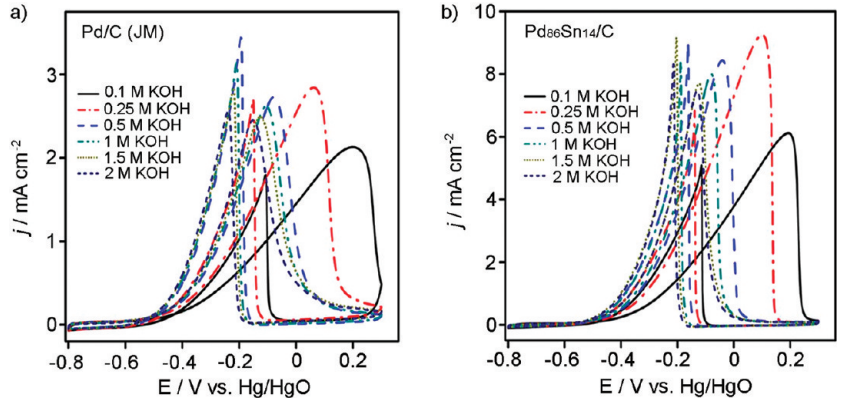

Figure 11. Cyclic voltammograms of (a) Pd/C (JM) and (b) $Pd_{86}Sn_{14}$/C in 0.5 M ethanol with varied KOH concentrations.

dx.doi.org/10.1021/cs2005955 | ACS Catal. 2012, 2, 287–297

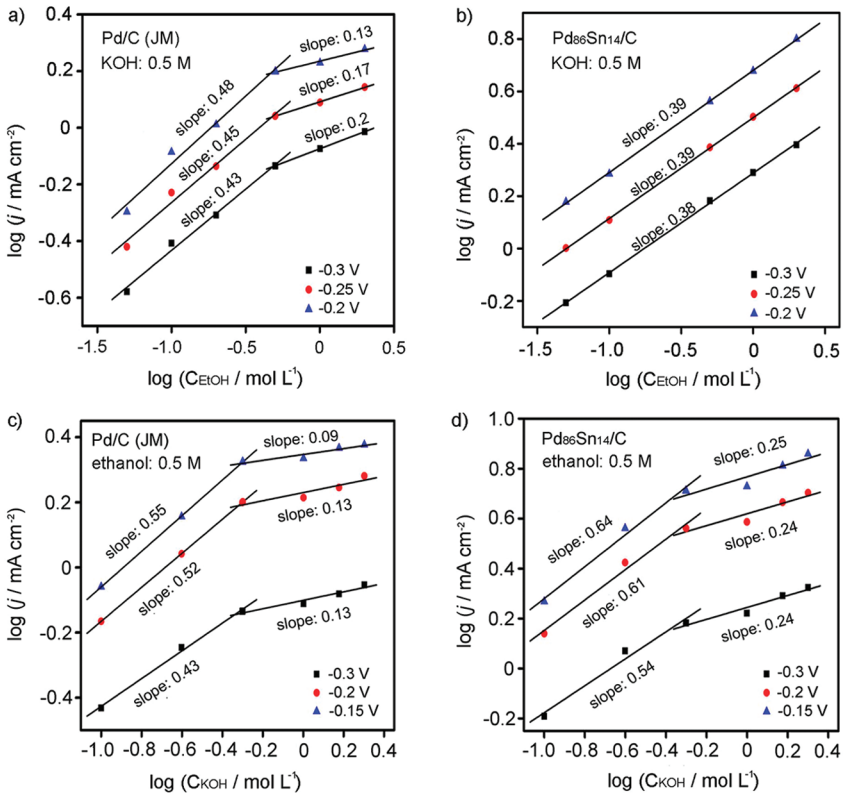

Figure 12. Plot of log j versus log $C_{ethanol}$ of (a) Pd/C (JM) and (b) $Pd_{86}Sn_{14}$/C in 0.5 M KOH (with varied ethanol concentration) and plot of log j versus log C_{KOH} of (c) Pd/C (JM) and (d) $Pd_{86}Sn_{14}$/C in 0.5 M ethanol (with varied KOH concentration). The current densities at different potentials in CV measurements were used for comparison.

constrained because of increased hydroxyl (*OH) coverage on the catalyst surface.

Since the acetic acid is the major product on the surface of Pd−Sn for the EOR in an alkaline medium, the rate-determining step is the removal of the adsorbed ethoxy ($*CH_3CO$) by the adsorbed hydroxyl (*OH), and the steady-state current from EOR and initial dehydrogenations of ethanol can be expressed as

$$i = 4FAk_b\Gamma_S\,\theta(CH_3CO)_{ads}\Gamma_S\,\theta(OH)_{ads} \quad (2)$$

$$M + OH^- \leftrightarrow M - (OH)_{ads} + e^- \quad (3)$$

$$Pd + CH_3CH_2OH \leftrightarrow Pd{-}(CH_3CH_2OH)_{ads} \quad (4)$$

$$Pd{-}(CH_3CH_2OH)_{ads} + 3M{-}(OH)_{ads} \rightarrow Pd{-}(CH_3CO)_{ads} + 3M + 3H_2O \quad (5)$$

where i is the current from the EOR at steady-state, "4" is the number of electrons being transferred upon the formation of acetic acid, F is the Faraday constant, A is the electrochemically active surface area (ECSA) of the Pd−Sn/C or Pd/C (JM) catalysts in this study, k_b is the reaction constant of the rate-determining-step ($CH_3CO + OH \rightarrow CH_3COOH$), Γ_S is the saturated adsorption amount, $\theta(CH_3CO)_{ads}$ is the coverage of the adsorbed CH_3CO, and $\theta(OH)_{ads}$ is the coverage of the adsorbed OH, M represents Pd or Sn metal. Although surface coverage of CH_3CO and OH are not clear in this study, eqs 3, 4, and 5 suggest that the coverage of adsorbed ethoxi (CH_3CO_{ads}) and OH_{ads} on the surface of Pd−Sn/C can be enhanced by increasing concentrations of ethanol and KOH (i.e., higher pH values).

To exclude the possibility that the charge-transfer rate (or reaction rate of EOR) is determined by mass transfer steps, we further calculated the mass-transfer-limited anodic current at RDE according to the Levich equation:

$$i_{l,a} = 0.62nFAD_0^{2/3}\omega^{1/2}\nu^{-1/6}C_{Ethanol} \quad (6)$$

If we substitute $i_{l,a} = j_{l,a}$ A into eq 6, where $j_{l,a}$ is the mass-transfer-limited current density, it can be rewritten as

$$j_{l,a} = 0.62nFD_0^{2/3}\omega^{1/2}\nu^{-1/6}C_{Ethanol} \quad (7)$$

where n is the number of electrons transferred, D_0 is diffusion coefficient of ethanol in aqueous solution, ω is angular frequency of rotation, ν is kinematic viscosity of solution. For simplification, we assume $n = 4$ (eq 1 is the major reaction that occurs at the electrode surface), $\nu \approx 0.01$ cm^2 s^{-1} (approximated as pure water at 20 °C since the aqueous KOH and ethanol solution is dilute) and take $D_0 \approx 10^{-5}$ cm^2 s^{-1},[48] $\omega = 2\pi \times 1000/60 = 104.7$ s^{-1}, $C_{ethanol} = 5 \times 10^{-4}$ mol cm^{-3}. By plugging these values into eq 7, we obtain $j_{l,a} \approx 1$ A cm^{-2} = 1000 mA cm^{-2}, which is much larger than the peak current density in the CV measurements for both Pd/C (JM) and $Pd_{86}Sn_{14}$/C catalysts. Therefore, it would be safe to neglect the contribution of mass transfer to the overall kinetics and consider the current we recorded to solely reflect the intrinsic reaction rate. A similar methodology was adopted to neglect the effect of mass transfer in other reported work .[49]

If we assume OH^- follows a Temkin type of adsorption and ethanol adsorption has a weak potential dependency during the potential range of −0.5 and −0.2 V, the overall anodic current density may be expressed as[45,50]

dx.doi.org/10.1021/cs2005955 | ACS Catal. 2012, 2, 287−297

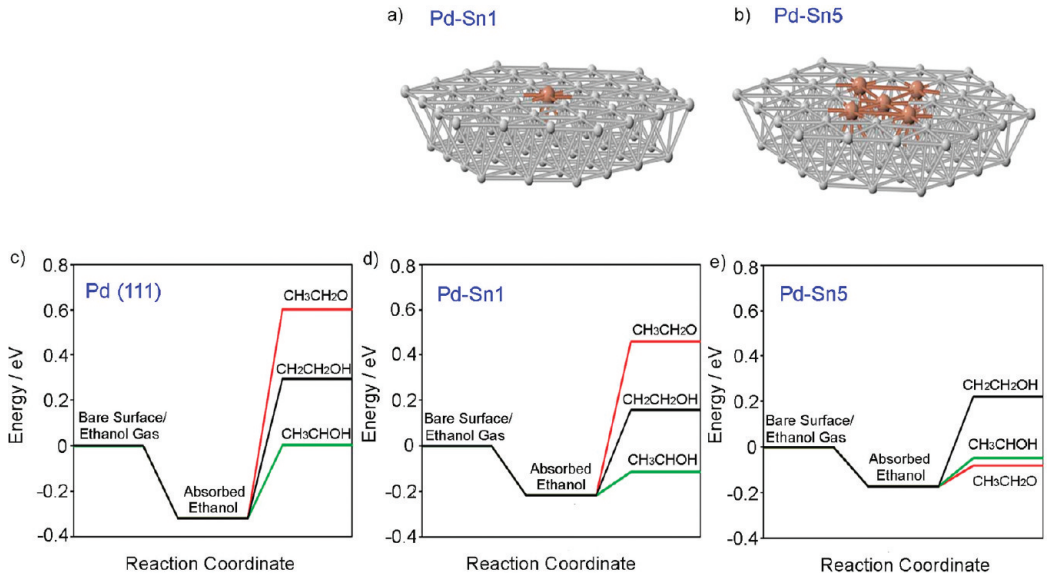

Figure 13. Surface cluster models of (a) Pd−Sn1 and (b) Pd−Sn5 used for modeling ethanol dehydrogenation, and reaction energies for H removal of ethanol over (c) Pd (111), (d) Pd−Sn1, (e) Pd−Sn5 surfaces. Lower energy values indicate more feasible reaction pathways.

$$j = nFR^* = nFkC^m_{\text{Ethanol}}C^s_{\text{KOH}}\exp\left(\frac{\alpha F}{RT}\eta\right) \quad (8)$$

$$\log(j) = \log(nFk) + m\log(C_{\text{Ethanol}}) + s\log(C_{\text{KOH}}) + \frac{\alpha F}{RT}\eta \quad (9)$$

where n is the number of electrons transferred in EOR, R* is reaction rate, k is reaction rate constant at room temperature, C is the bulk concentration of reactants (ethanol and OH^-), m is the overall reaction order of ethanol, s is the overall reaction order of OH^-, α is transfer coefficient, and η is overpotential (V). The coefficient $(RT)/(\alpha F)$ is the Tafel slope, and thus $(\alpha F)/(RT)$ is equal to 5.3 and 6.1 for Pd/C (JM) and $Pd_{86}Sn_{14}$/C catalysts, respectively.

By keeping KOH concentration constant (0.5 M), we further calculated the reaction order of ethanol ("m") by varying ethanol concentrations from 0.05 to 2 M and plotting log (j) versus log (C_{ethanol}) according to eq 10. Figure 12a shows that "m" for Pd/C (JM) presents distinct values (m = ∼0.45 and ∼0.17) when concentration of ethanol is below and above 0.5 M, respectively. On the other hand, "m" for $Pd_{86}Sn_{14}$/C shows a consistent value of ∼0.39 (Figure 12b), which may be attributed to the fact that Pd−Sn alloy has better OH^- adsorption ability than pure Pd. Such strong interaction between Sn and OH^- will enhance EOR activity even when concentrations of ethanol are higher than 0.5 M.

Similarly, by keeping the ethanol concentration constant (0.5 M) and varying the KOH concentration from 0.1 to 2 M, the reaction order of KOH ("s") can also be determined by analyzing the curves of log (j) versus log (C_{KOH}). For Pd/C (JM), "s" shows two distinct values ∼0.5 and ∼0.13 when the concentration of ethanol is below and beyond 0.5 M, respectively (Figure 12 c); on the other hand, for $Pd_{86}Sn_{14}$/C catalyst, "s" is equal to ∼0.6 and ∼0.25 when the concentration of ethanol is below and above 0.5 M, respectively (Figure 12 d).

Therefore, the overall rate law for Pd/C (JM) can be written as

$$j = 96500nkC^{0.45}_{\text{Ethanol}}C^{0.5}_{\text{KOH}}\exp(5.3\eta) \quad \text{when} \quad C_{\text{Ethanol}}, C_{\text{KOH}} \le 0.5\ \text{M} \quad (10)$$

$$j = 96500nkC^{0.17}_{\text{Ethanol}}C^{0.13}_{\text{KOH}}\exp(5.3\eta) \quad \text{when} \quad C_{\text{Ethanol}}, C_{\text{KOH}} \ge 0.5\ \text{M} \quad (11)$$

the overall rate law for $Pd_{86}Sn_{14}$/C

$$j = 96500n'k'C^{0.39}_{\text{Ethanol}}C^{0.13}_{\text{KOH}}\exp(6.1\eta) \quad \text{when} \quad C_{\text{Ethanol}}, C_{\text{KOH}} \le 0.5\ \text{M} \quad (12)$$

$$j = 96500n'k'C^{0.39}_{\text{Ethanol}}C^{0.25}_{\text{KOH}}\exp(6.1\eta) \quad \text{when} \quad C_{\text{Ethanol}}, C_{\text{KOH}} \ge 0.5\ \text{M} \quad (13)$$

Note n and n', k and k' are distinct from each other as they are in different catalytic reactions. The differences in reaction orders of C_{ethanol} and C_{KOH} between Pd/C (JM) and $Pd_{86}Sn_{14}$/C indicate the $Pd_{86}Sn_{14}$/C is a more favorable catalyst for EOR when C_{ethanol} and/or C_{KOH} are higher.

3.5. DFT Calculations. The reaction energies of the initial steps of the EOR (H removal) have also been studied over several catalysts using DFT: a Pd surface, a Pd−Sn1, and a Pd−Sn5 surface (Figure 13). The Pd−Sn1 and Pd−Sn5 surfaces had one and five Pd atoms replaced by Sn, respectively. The reaction was modeled by adsorbing ethanol (eq 14) from gas phase (ignoring the effect of the aqueous environment in these simplified calculations) and then removing an H atom from the adsorbed ethanol. These reactions are described below and involve removal of H from the O atom (eq 15), α−C atom (eq 16), or β−C atom (eq 17).

$$CH_3CH_2OH_{gas} \leftrightarrow CH_3CH_2OH_{ads} \quad (14)$$

$$CH_3CH_2OH_{ads} \leftrightarrow CH_3CH_2O_{ads} + H_{ads} \quad (15)$$

$$CH_3CH_2OH_{ads} \leftrightarrow CH_3CHOH_{ads} + H_{ads} \quad (16)$$

$$CH_3CH_2OH_{ads} \leftrightarrow CH_2CH_2OH_{ads} + H_{ads} \quad (17)$$

dx.doi.org/10.1021/cs2005955 | ACS Catal. 2012, 2, 287−297

The adsorption of the ethanol and various intermediates was found to usually be most stable on Pd atoms, rather than the Sn atoms. Sn enabled electronic and/or geometrical effects that changed the reaction energies over the predominantly Pd surface. For a few adsorbed species (ethanol and CH_3CH_2O over Pd−Sn1; and CH_3CH_2O over Pd−Sn5) adsorption over Sn atoms was preferred. The calculations showed that ethanol adsorption (eq 14) over Pd (111) is exothermic (−0.32 eV relative to gas phase), while H removal from α−C (eq 17) is endothermic (0.32 eV relative to adsorbed ethanol). Removal of H from O or the β−C over Pd are even more endothermic, being 0.91and 0.61 eV, respectively. On the other hand, H removal over the Pd−Sn1 cluster was less endothermic than over Pd (111), being 0.68, 0.10, and 0.38 eV for H removal from the O, α−C, and β−C, respectively (all relative to adsorbed ethanol). Dehydrogenation over Pd−Sn5 was also less endothermic than over Pd (111), having reaction energies of 0.10, 0.13, and 0.40 eV for H removal from the O, α−C, and β−C, respectively. Although our DFT calculations only involve the initial steps of EOR and do not reflect the complete picture of ethanol oxidation, they do agree with our experimental results in that they support the premise that Pd−Sn may be better catalysts than Pd for the EOR.

4. CONCLUSION

In this study, we successfully made a series of carbon supported Pd−Sn nanoparticles via a polyol method. In particular, we were able to identify the homogeneous alloy formation between Pd and Sn with the surface Sn being slightly oxidized in the $Pd_{86}Sn_{14}$/C electrocatalyst through combined characterization techniques. All the Pd−Sn/C catalysts demonstrated at least two times higher peak current densities (averaged by ECSA) compared to commercial Pd/C (JM) catalysts in CV measurements in 0.5 M ethanol + 0.5 M KOH solution, while only $Pd_{86}Sn_{14}$/C showed superior long-term stability compared to commercial Pd/C (JM) in chronoamperometry (CA) measurements. Tafel plot analysis revealed that all the Pd−Sn/C catalysts have lower Tafel slopes (139−162 mV dec^{-1}) than that of commercial Pd/C (JM) (187 mV dec^{-1}) and higher level of Sn content leads to a higher charge transfer rate during EOR. By comparing the cyclic voltammograms of $Pd_{86}Sn_{14}$/C with ethanol, acetaldehyde, and acetate as fuels, we conclude that the EOR on Pd−Sn catalysts might mainly proceed through partial oxidation of ethanol forming acetic acid. The overall dependence of both ethanol concentration and pH value for $Pd_{86}Sn_{14}$/C and commercial Pd/C (JM) catalysts in EOR were determined and compared, which indicates that $Pd_{86}Sn_{14}$/C is a more favorable catalyst for EOR under conditions of higher ethanol concentration and/or higher pH value. Our electrochemical measurements and DFT calculations highlight the promotional effect of Sn as an additive by forming a Pd−Sn binary alloy, and 14 at. % of Sn might be the optimal content. Future work may involve complete DFT calculations for EOR on Pd−Sn alloys and exploring a facile synthetic route to further decrease the size of the Pd−Sn nanoparticles, and thus enhance their electroactivity for the EOR more substantially in alkaline medium.

■ ASSOCIATED CONTENT

Supporting Information

TEM of Pd/C (homemade) and Pd/C (JM), and HAADF images and EELS line scans of $Pd_{86}Sn_{14}$ nanoparticles, CV and CA measurements of $Pd_{86}Sn_{14}$/C oxidized at 250 °C in the air for 1 h. This material is available free of charge via the Internet at http://pubs.acs.org.

■ AUTHOR INFORMATION

Corresponding Author

*Phone: 603-862-4245. Fax: 603-862-3747. E-mail: xw.teng@unh.edu.

Funding

This work is supported in part by the University of New Hampshire (X.T., W.D., K.M., D.M.). Research was carried out in part at the Center for Functional Nanomaterials, Brookhaven National Laboratory, which is supported by the U.S. Department of Energy, Office of Basic Energy Sciences, under Contract No. DE-AC02-98CH10886.

■ ACKNOWLEDGMENTS

We thank Sia Najafi at WPI for help in using WPI's computer clusters. We thank John Wilderman and Nancy Cherim at UNH for their assistance in XPS, TEM, and EDS measurements.

■ REFERENCES

(1) *Building a sustainable energy future: U.S. actions for an effective energy economy transformation*; National Science Board: Arlington, VA, 2009.
(2) Parsons, R.; Vandernoot, T. *J. Electroanal. Chem.* **1988**, *257*, 9−45.
(3) Acres, G. J. K. *J. Power Sources* **2001**, *100*, 60−66.
(4) Wyman, C. E. *Annu. Rev. Energy Environ.* **1999**, *24*, 189−226.
(5) Kheshgi, H. S.; Prince, R. C.; Marland, G. *Annu. Rev. Energy Environ.* **2000**, *25*, 199−244.
(6) Lave, L. B.; Griffin, W. M.; MacLean, H. *Issues Sci. Technol.* **2001**, *18*, 73−78.
(7) Joensen, F.; Rostrup-Nielsen, J. R. *J. Power Sources* **2002**, *105*, 195−201.
(8) Vielstich, W., Lamm, A., Gasteiger, H. A., Eds.; *Handbook of Fuel Cells: Fundamentals, Technology, Applications*. John Wiley & Sons Inc.: New York, 2004.
(9) de Souza, J. P. I; Queiroz, S. L.; Bergamaski, K.; Gonzalez, E. R.; Nart, F. C. *J. Phys. Chem. B* **2002**, *106*, 9825−9830.
(10) Kowal, A.; Li, M.; Shao, M.; Sasaki, K.; Vukmirovic, M. B.; Zhang, J.; Marinkovic, N. S.; Liu, P.; Frenkel, A. I.; Adzic, R. R. *Nat. Mater.* **2009**, *8*, 325−330.
(11) Vigier, F.; Coutanceau, C.; Hahn, F.; Belgsir, E. M.; Lamy, C. *J. Electroanal. Chem.* **2004**, *563*, 81−89.
(12) Bianchini, C.; Shen, P. K. *Chem. Rev.* **2009**, *109*, 4183−4206.
(13) Spendelow, J. S.; Wieckowski, A. *Phys. Chem. Chem. Phys.* **2007**, *9*, 2654−2675.
(14) Prakash, G. K. S.; Krause, F. C.; Viva, F. A.; Narayanan, S. R.; Olah, G. A. *J. Power Sources* **2011**, *196*, 7967−7972.
(15) Varcoe, J. R.; Slade, R. C. T.; Lam How Yee, E. *Chem. Commun.* **2006**, 1428−1429.
(16) Antolini, E.; Gonzalez, E. R. *J. Power Sources* **2010**, *195*, 3431−3450.
(17) Lamy, C.; Belgsir, E. M.; Leger, J. M. *J. Appl. Electrochem.* **2001**, *31*, 799−809.
(18) Ha, S.; Larsen, R.; Masel, R. I. *J. Power Sources* **2005**, *144*, 28−34.
(19) Coutanceau, C.; Demarconnay, L.; Lamy, C.; Leger, J. M. *J. Power Sources* **2006**, *156*, 14−19.
(20) Chen, Y. G.; Zhuang, L.; Lu, J. T. *Chin. J. Catal.* **2007**, *28*, 870−874.
(21) Xu, C. W.; Wang, H.; Shen, P. K.; Jiang, S. P. *Adv. Mater.* **2007**, *19*, 4256−+.
(22) He, Q. G.; Chen, W.; Mukerjee, S.; Chen, S. W.; Laufek, F. *J. Power Sources* **2009**, *187*, 298−304.

(23) Nguyen, S. T.; Law, H. M.; Nguyen, H. T.; Kristian, N.; Wang, S. Y.; Chan, S. H.; Wang, X. *Appl. Catal., B* **2009**, *91*, 507−515.
(24) Antolini, E.; Zignani, S. C.; Santos, S. F.; Gonzalez, E. R. *Electrochim. Acta* **2011**, *56*, 2299−2305.
(25) Kang, W. D.; Wei, Y. C.; Liu, C. W.; Wang, K. W. *Electrochem. Commun.* **2010**, *13*, 162−165.
(26) Lu, C. L.; Prasad, K. S.; Wu, H. L.; Ho, J. A. A.; Huang, M. H. *J. Am. Chem. Soc.* **2010**, *132*, 14546−14553.
(27) Antolini, E.; Gonzalez, E. R. *Catal. Today* **2011**, *160*, 28−38.
(28) Cui, G. F.; Song, S. Q.; Shen, P. K.; Kowal, A.; Bianchini, C. *J. Phys. Chem. C* **2009**, *113*, 15639−15642.
(29) *Handbook for Handling, Storing, and Dispensing E85*; U.S. Department of Energy: Washington, DC, 2010.
(30) Jiang, L. H.; Sun, G. Q.; Sun, S. G.; Liu, J. G.; Tang, S. H.; Li, H. Q.; Zhou, B.; Xin, Q. *Electrochim. Acta* **2005**, *50*, 5384−5389.
(31) Inada, H.; Wu, L. J.; Wall, J.; Su, D.; Zhu, Y. M. *J. Electron Microsc.* **2009**, *58*, 111−122.
(32) Jiang, L.; Colmenares, L.; Jusys, Z.; Sun, G. Q.; Behm, R. J. *Electrochim. Acta* **2007**, *53*, 377−389.
(33) Du, W. X.; Su, D.; Wang, Q.; Frenkel, A. I.; Teng, X. W. *Cryst. Growth Des.* **2011**, *11*, 594−599.
(34) Lippert, G.; Hutter, J.; Parrinello, M. *Mol. Phys.* **1997**, *92*, 477−487.
(35) VandeVondele, J.; Krack, M.; Mohamed, F.; Parrinello, M.; Chassaing, T.; Hutter, J. *Comput. Phys. Commun.* **2005**, *167*, 103−128.
(36) Goedecker, S.; Teter, M.; Hutter, J. *Phys. Rev. B* **1996**, *54*, 1703−1710.
(37) Krack, M. *Theor. Chem. Acc.* **2005**, *114*, 145−152.
(38) Perdew, J. P.; Burke, K.; Ernzerhof, M. *Phys. Rev. Lett.* **1996**, *77*, 3865−3868.
(39) Du, W. X.; Wang, Q.; Saxner, D.; Deskins, N. A.; Su, D.; Krzanowski, J. E.; Frenkel, A. I.; Teng, X. W. *J. Am. Chem. Soc.* **2011**, *133*, 15172−15183.
(40) Liu, Z. L.; Zhang, X. H. *Electrochem. Commun.* **2009**, *11*, 1667−1670.
(41) Casado-Rivera, E.; Volpe, D. J.; Alden, L.; Lind, C.; Downie, C.; Vazquez-Alvarez, T.; Angelo, A. C. D.; DiSalvo, F. J.; Abruna, H. D. *J. Am. Chem. Soc.* **2004**, *126*, 4043−4049.
(42) Antolini, E.; Gonzalez, E. R. *Electrochim. Acta* **2010**, *56*, 1−14.
(43) Du, W. X.; Wang, Q.; LaScala, C. A.; Zhang, L. H.; Su, D.; Frenkel, A. I.; Mathur, V. K.; Teng, X. W. *J. Mater. Chem.* **2011**, *21*, 8887−8892.
(44) Shen, P. K.; Xu, C. W. *Electrochem. Commun.* **2006**, *8*, 184−188.
(45) Liang, Z. X.; Zhao, T. S.; Xu, J. B.; Zhu, L. D. *Electrochim. Acta* **2009**, *54*, 2203−2208.
(46) Bianchini, C.; Bambagioni, V.; Filippi, J.; Marchionni, A.; Vizza, F.; Bert, P.; Tampucci, A. *Electrochem. Commun.* **2009**, *11*, 1077−1080.
(47) Zhou, Z. Y.; Wang, Q. A.; Lin, J. L.; Tian, N.; Sun, S. G. *Electrochim. Acta* **2010**, *55*, 7995−7999.
(48) Pratt, K. C.; Wakeham, W. A. *Proc. R. Soc. A* **1974**, *336*, 393−406.
(49) Hitmi, H.; Belgsir, E. M.; Leger, J. M.; Lamy, C.; Lezna, R. O. *Electrochim. Acta* **1994**, *39*, 407−415.
(50) Tripkovic, A. V.; Popovic, K. D.; Momcilovic, J. D.; Drazic, D. M. *J. Electroanal. Chem.* **1996**, *418*, 9−20.